

High-Resolution Large-Area Digital Orthophoto Map Generation Using LROC NAC Images

Kaichang Di, Mengna Jia, Xin Xin, Jia Wang, Bin Liu, Jian Li, Jianfeng Xie, Zhaoqin Liu, Man Peng, Zongyu Yue, Jia Liu, Ruilin Chen, and Changlu Zhang

Abstract

The Chang'e-5 mission of China is planned to be launched in 2019 to the landing area near Mons Rümker located in Oceanus Procellarum. Aiming to generate a high-resolution and high-quality digital orthophoto map (DOM) of the planned landing area for supporting the mission and various scientific analyses, this study developed a systematic and effective method for large-area seamless DOM production. The mapping results of the Chang'e-5 landing area using over 700 Lunar Reconnaissance Orbiter Camera (LROC) Narrow Angle Camera (NAC) images are presented. The resultant seamless DOM has a resolution of 1.5 m, covers a large area of 20° in longitude and 4° in latitude, and is tied to SLDDEM2015. The results demonstrate that the proposed method can reduce the geometric inconsistencies among the LROC NAC images to the subpixel level and the positional errors with respect to the reference digital elevation model to about one grid cell size.

Introduction

Mapping of the lunar surface using orbital imagery is one of the fundamental tasks of almost every lunar orbiter mission. Among the common mapping products, digital orthophoto maps (DOMs) are essential for measuring and characterizing lunar surface features. Thus, they are usually used as the base map for morphological and geological analysis (Wu *et al.* 2014; Zhang *et al.* 2016; Yue *et al.* 2017). High-resolution and high-precision DOMs are particularly important for supporting lander and rover missions in terms of landing site analysis, safe landing, and surface operations.

China started the Lunar Exploration Program in 2004, which consists of orbital, soft lander/rover, and sample return missions (Ouyang *et al.* 2004). The first two phases were achieved by the Chang'e-1, Chang'e-2, and Chang'e-3 missions, and the third phase (i.e., sample return mission) will be realized by the Chang'e-5 mission in 2019. The Chang'e-5 mission aims to return about 2 kg of lunar soil and rock samples. Its target area is near Mons Rümker located in Oceanus Procellarum, which is a large area of lunar mare on the northwest region of the Moon (Gbtimes 2017). High-resolution and high-precision mapping of the landing area is critical to support overall mission planning and detailed analysis of

potential sampling sites (Haase *et al.* 2012; Wu *et al.* 2014; Kokhanov *et al.* 2017).

So far, there are a number of lunar global orbital image mosaic maps available, such as Clementine global mosaic (100 m/pixel) (Robinson *et al.* 1999), Lunar Reconnaissance Orbiter Camera (LROC) Wide Angle Camera (WAC) globe mosaic (100 m/pixel) (Arizona State University [ASU] 2011; National Aeronautics and Space Administration [NASA] 2011; Wagner *et al.* 2015), Chang'e-1 CCD camera global mosaic (120 m/pixel) (Li *et al.* 2010), and Chang'e-2 CCD camera global mosaic (7 m/pixel) (Data Publishing and Information Service System of China Lunar Exploration Project 2018; Li *et al.* 2015). However, these products are not sufficient for detailed landing site analysis due to their low resolutions.

The highest-resolution lunar orbital imagery is achieved by the LROC Narrow Angle Camera (NAC), and the images covered nearly the entire lunar surface at a resolution of 0.5–2.0 m. However, there are only a limited number of high-resolution featured mosaics (Klem *et al.* 2014) and digital elevation model (DEM) products (Tran *et al.* 2010; Burns *et al.* 2012) that have been released by the LROC team. The number of images used in most featured mosaics is from two to tens of NAC images. The largest LROC NAC mosaic at present is the LROC Northern Polar Mosaic (<http://lroc.sese.asu.edu/images/gigapan>; NASA/Goddard Space Flight Center/ASU 2014; Wagner *et al.* 2015, 2016), which contains 10 581 NAC images, covering an area from 60°N to the north pole at a resolution of 2 m. However, apparent geometric inconsistencies of up to ~7 pixels were observed due to problems of the designed procedure (Archinal *et al.* 2015). Nevertheless, this product does not cover the Chang'e-5 planned landing area. The spatial coverage of publicly available high-resolution DOMs is very limited. Overall, it is highly desirable to develop effective techniques for large-area high-precision seamless DOM generation.

Photogrammetric processing of high-resolution orbital images for lunar surface mapping has been performed using different software systems or methods, such as the US Geological Survey (USGS) Integrated System for Imagers and Spectrometers (ISIS), SOCET SET, NASA Ames Stereo Pipeline (Moratto *et al.* 2010), and in-house-developed methods. Tran *et al.* (2010) and Burns *et al.* (2012) generated digital terrain models (DTMs) by LROC NAC stereo images with the SOCET SET software. The resultant DTMs have a typical spatial sampling of 2 m and a vertical precision of 1–2 m (Burns *et al.* 2012); the root mean square (RMS) residuals are typically ~0.25 pixels for a pair of NAC stereo images and less than 1 pixel for multiple sets of stereo images (Tran *et al.* 2010). Klem *et al.* (2014) produced a controlled mosaic for LROC NAC images using the USGS ISIS software, and the seam precision for the mosaics was generally within 7–8 pixels. Lee *et al.* (2012) and

Kaichang Di, Bin Liu, Zhaoqin Liu, Man Peng, Zongyu Yue, Ruilin Chen, and Changlu Zhang are with the State Key Laboratory of Remote Sensing Science, Institute of Remote Sensing and Digital Earth, Chinese Academy of Sciences, Beijing 100101, China (liubin@radi.ac.cn).

Mengna Jia, Xin Xin, and Jia Liu are with the State Key Laboratory of Remote Sensing Science, Institute of Remote Sensing and Digital Earth, Chinese Academy of Sciences, Beijing 100101, China; and the University of Chinese Academy of Sciences, Beijing 100049, China.

Jia Wang, Jian Li, and Jianfeng Xie are with the Beijing Aerospace Control Center, Beijing, 100094, China.

Photogrammetric Engineering & Remote Sensing
Vol. 85, No. 7, July 2019, pp. 481–491.
0099-1112/19/481–491

© 2019 American Society for Photogrammetry
and Remote Sensing
doi: 10.14358/PERS.85.7.481

Archinal *et al.* (2015) used USGS ISIS to generate controlled polar mosaics from LROC NAC images. The residuals were within 1 pixel with a maximal error of ~ 7 pixels, and the horizontal accuracy of the mosaics was within 100 m with respect to the Lunar Orbiter Laser Altimeter (LOLA) data (Lee *et al.* 2012).

Wu *et al.* (2014) developed a combined block adjustment method to process Chang'e-2 stereo imagery and LOLA data of the Chang'e-3 landing area. The resultant DTM has an average elevation difference of 15.19 m and a standard deviation of 17.08 m compared to that of the LOLA DEM. Di *et al.* (2014) developed a self-calibration bundle adjustment method for Chang'e-2 stereo images to reduce the georeferencing inconsistencies among the images of adjacent orbits from up to 20 pixels to a subpixel level. Kokhanov *et al.* (2017) used a self-developed photogrammetric method to obtain cartographic products of potential landing sites for the "Luna-25" mission from 11 LROC NAC stereo pairs. The bundle adjustment results had precisions of 0.3 m and 1.0 m in the planar direction and 3.5 m in the vertical direction. Haase *et al.* (2012, 2014) produced a DTM and ortho-mosaic for the Apollo-17 landing site using LROC NAC stereo images. The LROC-adapted German Aerospace Center photogrammetric processing chain was used for stereo image processing, and the resultant DTM had a standard deviation of 40 cm in elevational difference with the LOLA profiles.

As previously described, existing lunar mapping research is generally based on stereo images. However, the LROC NACs can only acquire stereo images from adjacent orbits using off-nadir slew in limited interested locations, and most of the time, the captured NAC images have nadir orientation. There are only a few NAC stereo pairs in the Chang'e-5 planning landing area because the nadir NAC images cannot be used to generate a high-resolution DOM mosaic using stereo photogrammetric methods. Furthermore, most of the existing studies have been focused on photogrammetric processing involving several or tens of images. For large-area mapping, the geometric and radiometric inconsistencies are more severe and complicated. Therefore, it is necessary to develop a more effective method to produce high-precision DOM mosaics for large areas using nonstereo NAC images and a lunar control source of limited resolution.

This research aimed to develop a systematic and effective method for generating a seamless DOM for the planned Chang'e-5 landing area. In this work, we used a two-step strategy. First, the study area was divided into several overlapped subareas, and a planar block adjustment with control points was applied to each subarea to lower the geometric deviations among the NAC images to the subpixel level at the same time of tying the NAC images to the reference SLDEM2015. Then a seamless DOM mosaic of each subarea was generated. Second, the thin plate spline (TPS) model (Wahba 1990) was applied to the subarea DOMs to remove the positional inconsistencies between the adjacent subarea DOMs and guarantee seamless DOM mosaicking throughout the whole research area. Using the proposed two-step method, a controlled seamless mosaic of the Chang'e-5 landing area was created with high geometric precision and with a resolution of 1.5 m.

Data

The planned landing area of Chang'e-5 mission was chosen to verify the proposed large-area DOM generation method. It locates near Mons Rümker within Oceanus Procellarum and covers an area of approximately 20° longitude \times 4° latitude, or approximately $413.8 \text{ km} \times 121.4 \text{ km}$ (Di *et al.* 2018). LROC NAC images were the data source used in this research. SLDEM2015, a combined product of LOLA laser altimetry and DEMs generated from the Japanese Selenological and Engineering Explorer (SELENE) terrain camera images (Barker *et al.* 2016), was used as reference DEM for ortho-rectification. Figure 1 shows the planned landing area of Chang'e-5 on the LROC WAC mosaic.

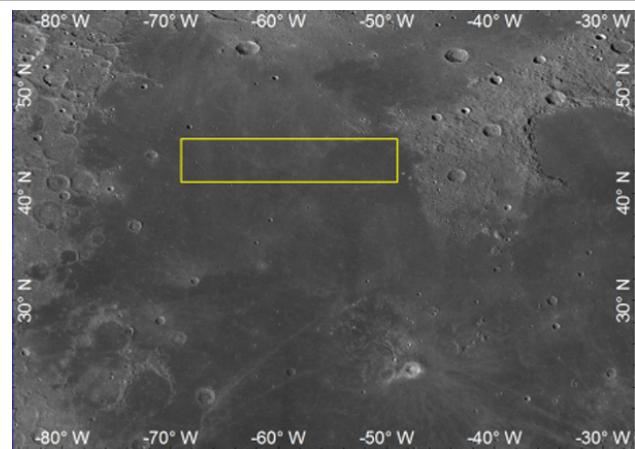


Figure 1. Planned landing area of Chang'e-5 marked as a rectangle on the LROC WAC mosaic.

LROC NAC Images

The LROC is a system of three cameras onboard the Lunar Reconnaissance Orbiter (LRO) that captures high-resolution monochromatic images and moderate-resolution multispectral images of the lunar surface. It consists of two NACs that are designed to provide 0.5–2.0 m/pixel monochromatic narrow-angle line scan images and a WAC that provides images at a scale of 100 m/pixel in seven color bands over a 60-km swath (Robinson *et al.* 2010).

NAC Experimental Data Record images were downloaded from the NASA Planetary Data System (PDS) and preprocessed using the USGS ISIS software. SPICE kernels (NAIF 2014) were attached to each image using the "spiceinit" command, and radiometric corrections and removal of echo effects were realized by the "Ironaccal" command and the "Ironacecho" command, respectively (PDS 2014; Henriksen *et al.* 2016). Until December 2017, the planned Chang'e-5 landing area is covered by about 2299 LROC NAC images. Considering the illumination conditions, most of the chosen images have similar solar azimuth angles that are higher than 180° (afternoon images) and incidence angles between 40° and 80° . The planned landing area could not be completely covered with afternoon images, so small gaps were filled with one or two morning images. A total of 765 NAC images were involved in this research with a ground sample distance of mainly 1.5 m.

Control Source

SLDEM2015 was used as the control source for providing three-dimensional control points in the block adjustment stage as well as providing topographic correction during DOM generation. This product is a lunar shape model generated by a combination of LOLA and SELENE data. This includes 43 200 stereo-derived DEMs from SELENE Terrain Camera images and 4.5 billion surface heights from LOLA (Barker *et al.* 2016). The resultant near-global lunar DEM has an effective resolution of approximately 60 m at the equator and a typical vertical accuracy of approximately 3–4 m. In addition, the LROC WAC mosaic (NASA 2011; Wagner *et al.* 2015) was used as a reference for grayscale balancing in the image mosaicking process.

Method for Large-Area Controlled DOM Generation

In this research, a two-stage method was used to generate a large-area controlled seamless DOM. Figure 2 is the flowchart showing the generation process of large-area seamless DOM. To guarantee both the processing efficiency and mapping precision, the large landing area was partitioned into 10 subareas and processed in parallel. Dividing the whole mapping area into some subareas is a common strategy when dealing with

large-area or global mapping, especially in the planetary mapping field (Gwinner *et al.* 2010, 2016; Preusker *et al.* 2017). Mapping with partitions is an engineering method for parallel processing and dealing with huge amounts of data. It is also a feasible way to improve the processing precision when the data are of different quality in different regions, which is very common with the planetary orbital images (Gwinner *et al.* 2016).

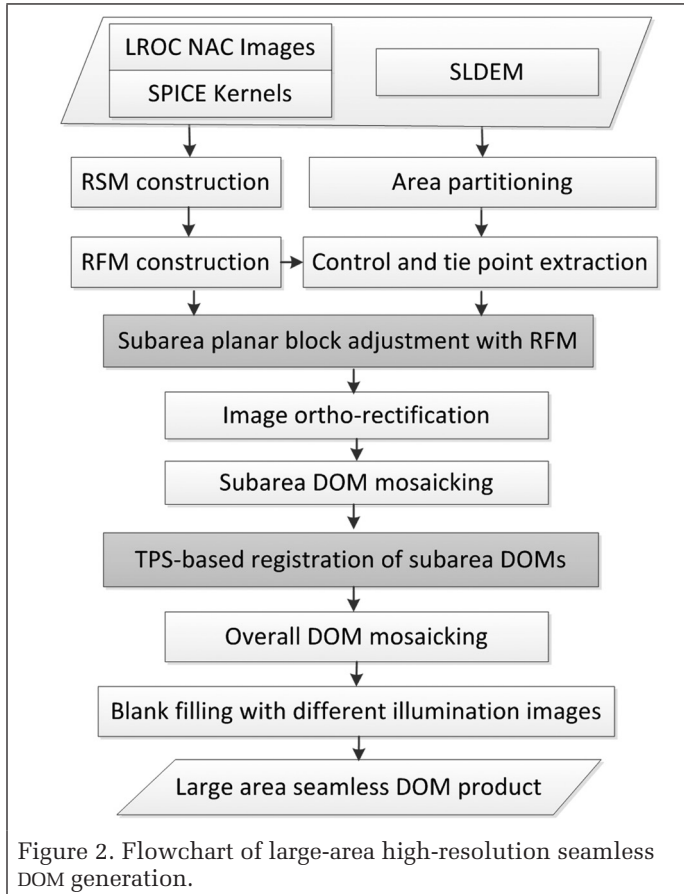


Figure 2. Flowchart of large-area high-resolution seamless DOM generation.

A planar block adjustment with control points was used in each subarea to ensure the relative consistency among the LROC NAC images and the absolute accuracy to the control source. The rational function model (RFM) of the image was refined during the block adjustment. Via the block adjustment, geometric inconsistencies between adjacent LROC NAC images within each subarea can be effectively reduced. Subsequently, the DOM of each image was automatically generated, and the DOMs within each subarea were mosaicked together. Because of the resolution limitation of the reference source, some positional inconsistencies between the DOM mosaics of neighboring subareas remained. Therefore, a TPS model-based image registration was applied to the generated subarea DOM mosaics. To maintain the grayscale and contrast homogeneity, a histogram matching-based grayscale balancing method was applied to all the DOMs. Finally, a seamless DOM product of the entire planned landing area was generated via mosaicking.

It is worth mentioning that the contrast of the WAC mosaic is lower than most NAC images, which causes the NAC mosaic to appear a little grayish. Nevertheless, the WAC mosaic provides a very consistent source in a larger scale so that the produced mosaic has a good radiometric consistency, which can satisfy most of the applications at present. Color balancing for large-area mapping deserves future research.

Geometric Models of Orbital Imagery

The geometric model of the imagery is the mathematical basis for block adjustment as well as the image ortho-rectification. It builds the relationship between object-space coordinates and image-space coordinates.

The rigorous sensor model (RSM) of an image represents the imaging process by collinearity equations with interior orientation (IO) parameters and exterior orientation (EO) parameters (Di *et al.* 2014; Henriksen *et al.* 2016; Liu *et al.* 2017). The generic geometric model of an image fits the relationship between the image and ground coordinates via mathematical functions, the parameters of which have no physical meaning related to the imaging process. The most commonly used generic geometric model is the RFM. The RFM has the advantages of high fitting precision, simple and uniform form, high calculation speed, and imaging sensor independence. It has already been widely accepted that the RFM can approximate the RSM at a precision of 1/100 pixel in image space (Liu *et al.* 2016, 2017) such that it can be used to replace RSM without a loss of accuracy.

The RSM of the NAC imagery was constructed using the IO and EO parameters recorded in SPICE kernels (NAIF 2014). It can be generally described (Di *et al.* 2014) as

$$\begin{bmatrix} X - X_s \\ Y - Y_s \\ Z - Z_s \end{bmatrix} = \lambda R_{ol} R_{bo} R_{ib} \begin{bmatrix} x \\ y \\ -f \end{bmatrix} = \lambda R \begin{bmatrix} x \\ y \\ -f \end{bmatrix} \quad (1)$$

where (x, y) are the focal plane image coordinates; f is the focal length; (X, Y, Z) and (X_s, Y_s, Z_s) represent the lunar-surface-point coordinates and the position of optical center in the lunar body-fixed coordinate system (LBF), respectively; λ is a scale factor; R_{ib} is the rotational matrix from the image space coordinate system to the spacecraft body coordinate system (BCS); R_{bo} is the rotational matrix from the BCS to the orbit coordinate system (OCS); R_{ol} is the rotational matrix from the OCS to the LBF; and R is the combination of these three rotation matrices and can be constructed using the three EO angle parameters (ω, ϕ, κ) (Liu *et al.* 2017).

In principle, for linear array push-broom images, each line has a different set of EO parameters. Because the time interval of the orbit measurement is much longer than that of the line scanning, only a small portion of the image lines have EO parameters from direct measurements. To obtain the EO parameters of all image lines via interpolation, the EO parameters are usually interpolated with respect to the scan time t (Di *et al.* 2014). There are many methods for EO parameter interpolation. The polynomial representation is a feasible choice and widely used. The third-order polynomial is chosen to model the EO parameters as shown in Equation 2:

$$\begin{aligned} X_s(t) &= a_0 + a_1 t + a_2 t^2 + a_3 t^3 \\ Y_s(t) &= b_0 + b_1 t + b_2 t^2 + b_3 t^3 \\ Z_s(t) &= c_0 + c_1 t + c_2 t^2 + c_3 t^3 \\ \phi(t) &= d_0 + d_1 t + d_2 t^2 + d_3 t^3 \\ \omega(t) &= e_0 + e_1 t + e_2 t^2 + e_3 t^3 \\ \kappa(t) &= f_0 + f_1 t + f_2 t^2 + f_3 t^3 \end{aligned} \quad (2)$$

where a_0, a_1, \dots, f_3 are the polynomial coefficients of the six EO parameters $(X_s, Y_s, Z_s, \omega, \phi, \kappa)$.

The focal plane image coordinates (x, y) can be obtained by transforming from the image coordinates (*row, sample*) using IO parameters as follows:

$$x_d = (\text{sample} - \text{BORESIGHT_SAMPLE}) \cdot \text{PIXEL_PITCH} \quad (3)$$

$$r = x_d \quad (4)$$

$$x = x_d / (1 + k_1 \cdot r^2) \quad (5)$$

where *PIXEL_PITCH* is the pixel size of the image, *BORESIGHT_SAMPLE* is the principal point coordinate, x_d is the distorted position (the measured position), r is the distance between the optical center and image point, k_1 is the distortion coefficient, and x is the corrected focal plane position in millimeters (mm). The IO parameters of the left and right cameras (NAC-L and NAC-R) can be found in the SPICE kernels of the LRO mission. The NAC cameras are line scanners (single-line CCD); y_d is unmeasured and probably unimportant, and thus y is assumed to be zero according to the LROC Instrument Kernel file (NAIF 2014; Liu *et al.* 2017).

The RFM is represented as the ratio of the polynomials shown in Equation 6 as follows:

$$\begin{aligned} r_n &= \frac{P_1(X_n, Y_n, Z_n)}{P_2(X_n, Y_n, Z_n)} \\ c_n &= \frac{P_3(X_n, Y_n, Z_n)}{P_4(X_n, Y_n, Z_n)} \end{aligned} \quad (6)$$

where (r_n, c_n) and (X_n, Y_n, Z_n) are the normalized image coordinates and ground coordinates, respectively. The third-order polynomial P_i ($i = 1, 2, 3,$ and 4) has a general form as follows:

$$\begin{aligned} P_i(X_n, Y_n, Z_n) &= a_1 + a_2 X_n + a_3 Y_n + a_4 Z_n + a_5 X_n Y_n + a_6 X_n Z_n + a_7 Y_n Z_n + a_8 X_n^2 \\ &+ a_9 Y_n^2 + a_{10} Z_n^2 + a_{11} X_n Y_n Z_n + a_{12} X_n^3 + a_{13} X_n Y_n^2 + a_{14} X_n Z_n^2 + a_{15} X_n^2 Y_n + a_{16} Y_n^3 \\ &+ a_{17} Y_n Z_n^2 + a_{18} X_n^2 Z_n + a_{19} Y_n^2 Z_n + a_{20} Z_n^3 \end{aligned} \quad (7)$$

where $a_1, a_2 \dots$ to a_{20} are the coefficients of the polynomial function P_i , named rational polynomial coefficients (RPCs).

The RFM of the LROC NAC imagery was established by least-squares fitting with a large number of virtual control points generated by RSM of the image (Di *et al.* 2018). A series of grid points in a certain interval were created first in every image as the virtual control points in image space, after which the elevation in the object space was divided into several layers and the planar ground coordinates of the virtual control points in every layer were calculated using the RSM. Finally, the RPCs were derived using these virtual control points via least-squares fitting (Liu *et al.* 2017).

Subarea Planar Block Adjustment

The accuracy of the constructed RSM of LROC NAC imagery depends on the accuracy of the orbit and attitude of the LRO. Consequently, the fitted RFM also contains errors at the same level as that of the RSM. Benefiting from lunar gravity field data of the Gravity Recovery and Interior Laboratory mission, the LRO orbit determination obtained an accuracy of ~20 m. The accuracy was further improved to ~14 m after incorporating crossovers of LOLA data (Mazarico *et al.* 2012). The errors of the RSMs and RFMs of the images cause positional deviations of adjacent rectified images that should be reduced to a subpixel level to better support engineering and science applications.

Photogrammetric block adjustment is an effective means to improve the geopositioning accuracy of a geometric model (Gwinner *et al.* 2010; Wu and Liu 2017). Traditionally, three-dimensional ground coordinates of the tie points are solved using stereo block adjustment. However, if the stereo convergence angle is very small (e.g., <10°), the normal equations of the block adjustment will be ill-conditioned, and as a result, the calculated ground height will be abnormal. This is widespread in our experiments because of the lack of coverage of stereo LROC NAC pairs.

The traditional DOM registration is also a widely used method to remove the geometric deviations between images with low convergence angles. This is usually accomplished with the help of high-precision control data. However, the lack of high-precision control data of the lunar surface limits the registration precision. It is hard to make the NAC DOMs geometric seamless by using the traditional registration method with control points from presently available DOM mosaics or DEMs.

To resolve the problem, a DEM-aided planar block adjustment was developed to refine the RFMs of the LROC NAC images. In order to ortho-rectify the LROC NAC images and support collaborative analysis of produced DOM mosaic and existing DEM in various science applications, the geometric models of the images should be corresponded to the reference DEM. Thus, in each subarea block adjustment, a few control points were manually selected using SLDEM2015 as the reference. The control points are mostly centers of small craters and are evenly distributed in the research area. The extracted feature points in every NAC image are matched automatically to obtain tie points. After that, the distribution of tie points is checked carefully to ensure that every overlapping area has evenly distributed points. If such a condition is not satisfied, manually selected tie points will be used. Most of the NAC images (750 out of 765 images used) were taken in the afternoon and have similar illumination conditions, and they can be automatically matched for tie point selection. A very small number of images (15) were taken in the morning and have severe illumination differences with neighboring images taken in the afternoon, and manual selection is necessary to obtain tie points in these images. Image matching under different illumination condition is still a challenging issue. Recently, Wu *et al.* (2018) have done some related work in automatic matching of planetary images using illumination-invariant feature points. The issue is worth of further study to make the adjustment process more efficient.

The error equations of the block adjustment are shown in Equation 8. Compared to stereo block adjustment, planar block adjustment is a method that calculates only the tie point ground plane coordinates, while the elevation coordinates can be interpolated from a DEM. In the block adjustment, the affine transformation model in image space (Equation 8) is used to compensate the systematic errors rather than recalculating the RPCs:

$$\begin{aligned} F_x &= e_0 + e_1 \cdot \text{sample} + e_2 \cdot \text{line} - x \\ F_y &= f_0 + f_1 \cdot \text{sample} + f_2 \cdot \text{line} - y \end{aligned} \quad (8)$$

where the image coordinates acquired by back-projecting the ground coordinates with the RFM (as shown in Equation 6) are represented by *sample* and *line*, while the measured image coordinates are shown as x and y ; e_0, e_1, e_2 are the affine transformation parameters in the sample direction, and f_0, f_1, f_2 are the affine transformation parameters in the line direction.

Because the error equations of planar block adjustment are nonlinear relative to the ground coordinates, a Taylor series expansion is used to linearize the error equations as shown in Equation 9. The unknowns to be solved include the tie point ground planar coordinates (lat, lon) and the affine transformation model parameters as shown in Equation 9. The elevation coordinates are interpolated from a DEM iteratively:

$$\begin{aligned} v_x &= \frac{\partial F_x}{\partial e_0} \cdot \Delta e_0 + \frac{\partial F_x}{\partial e_1} \cdot \Delta e_1 + \frac{\partial F_x}{\partial e_2} \cdot \Delta e_2 + \frac{\partial F_x}{\partial lat} \cdot \Delta lat + \frac{\partial F_x}{\partial lon} \cdot \Delta lon - l_x \\ v_y &= \frac{\partial F_y}{\partial f_0} \cdot \Delta f_0 + \frac{\partial F_y}{\partial f_1} \cdot \Delta f_1 + \frac{\partial F_y}{\partial f_2} \cdot \Delta f_2 + \frac{\partial F_y}{\partial lat} \cdot \Delta lat + \frac{\partial F_y}{\partial lon} \cdot \Delta lon - l_y \end{aligned} \quad (9)$$

The error equations for control points are shown in Equation 10, and only the affine transformation parameters need to be calculated for control points:

$$\begin{aligned} v_x &= \frac{\partial F_x}{\partial e_0} \cdot \Delta e_0 + \frac{\partial F_x}{\partial e_1} \cdot \Delta e_1 + \frac{\partial F_x}{\partial e_2} \cdot \Delta e_2 - I_x \\ v_y &= \frac{\partial F_y}{\partial f_0} \cdot \Delta f_0 + \frac{\partial F_y}{\partial f_1} \cdot \Delta f_1 + \frac{\partial F_y}{\partial f_2} \cdot \Delta f_2 - I_y \end{aligned} \quad (10)$$

The error equations of each control point and tie point can be constructed using Equations 9 and 10. The unknown parameters can be calculated iteratively using the least-squares algorithm until the termination condition of iteration is satisfied.

In this research, the planar block adjustment was conducted in each subarea independently. Using the RPCs and the calculated affine transformation parameters, the NAC images were ortho-rectified with respect to SLDEM2015, through which the image distortions caused by topographic relief and the imprecision of the original EO parameters were simultaneously corrected. Finally, the subarea seamless DOM mosaic was produced using the individual DOMs within the subarea.

TPS-Based Large-Area Image Registration

The planar block adjustment can remove the geometric deviations among images within each subarea, but inconsistencies remain among the subarea DOM mosaics because of the limited control precision. Therefore, registration between subarea mosaics is needed to eliminate the residual geometric inconsistencies. We propose a novel method of TPS model-based large-area image registration to seamlessly register the subarea DOMs while simultaneously maintaining mapping accuracy.

The TPS model is an effective technique for data interpolation and smoothing and has been widely used in image alignment, shape matching, image warping, spatial data interpolation, and other circumstances that require the modeling of nonrigid deformation. As shown in Equation 11, the TPS model consists of an affine transformation model and a distance-related quantity that indicates that the impact of the control point on the interpolation point depends on the distance between them:

$$f(x, y) = \alpha_0 + \alpha_1 x + \alpha_2 y + \sum_{(j=1)}^m \delta_j \psi(r_j) \quad (11)$$

where the quantity of control points are represented by m and r_j is the Euclidean distance from the j th control point (x_j, y_j) to an arbitrary image point (x, y) as follows:

$$r_j = \sqrt{(x - x_j)^2 + (y - y_j)^2} \quad (12)$$

where ψ is the radial-basis-function kernel

$$\psi(r) = \begin{cases} r^2 \log(r), & r \neq 0 \\ 0, & r = 0 \end{cases} \quad (13)$$

and $\alpha_0, \alpha_1, \alpha_2$, and δ_j in Equation 12 are the coefficients that should be calculated by minimizing the weighted sum of the error measure $E(f)$ (Equation 15) and roughness measure $R(f)$ (Equation 16) (Di *et al.* 2018) as follows:

$$\min(E(f) + \lambda R(f)) \quad (14)$$

$$E(f) = \sum_{(j=1)}^m \|z_j - f(x_i, y_j)\|^2 \quad (15)$$

$$R(f) = \iint \left(\left(\frac{\partial^2 f}{\partial^2 x^2} \right)^2 + 2 \left(\frac{\partial^2 f}{\partial x \partial y} \right)^2 + \left(\frac{\partial^2 f}{\partial^2 y^2} \right)^2 \right) dx dy \quad (16)$$

where λ represents a smoothing parameter that is required to be nonnegative. If $\lambda = 0$, there will be no smoothness constraint, and all the control points are exactly passed through when fitting the TPS model. Otherwise, if $\lambda = +\infty$, the coefficient δ becomes a zero vector, and the TPS model will turn into an affine transformation model (Shen *et al.* 2017). The variable λ was set to be zero in our experiment so that the registration precision can reach as high a level as possible for the control point pairs and the surrounding area. It is also a guarantee for the subsequent registration process to be implemented simultaneously.

When registering the subarea DOMs with the TPS model, a subarea DOM in the central part of the whole area was used as the reference for neighboring DOMs. Then the registered DOMs become new references for subsequent subarea mosaics until all the subarea DOMs are registered.

For DOM registration, the TPS coefficients are calculated by the matched reference control points and auxiliary control points. The reference control points are the matched points between the target DOM and the reference DOM, while the auxiliary control points are on the opposite-side margin of the target DOM, which are introduced to constrain the geometric error in the local area and avoid overcorrection of the DOM. For example, in Figure 3, the subarea DOM labeled “Left DOM” needs to be registered to the “Reference DOM,” so the reference control points were on the right margin of the “Left DOM,” shown as circles, while the auxiliary control points were marked as crosses and distributed on the left margin of the “Left DOM.” Consequently, when solving TPS coefficients, the reference control point coordinates of the target DOM were corrected with respect to the reference DOM. The coordinates

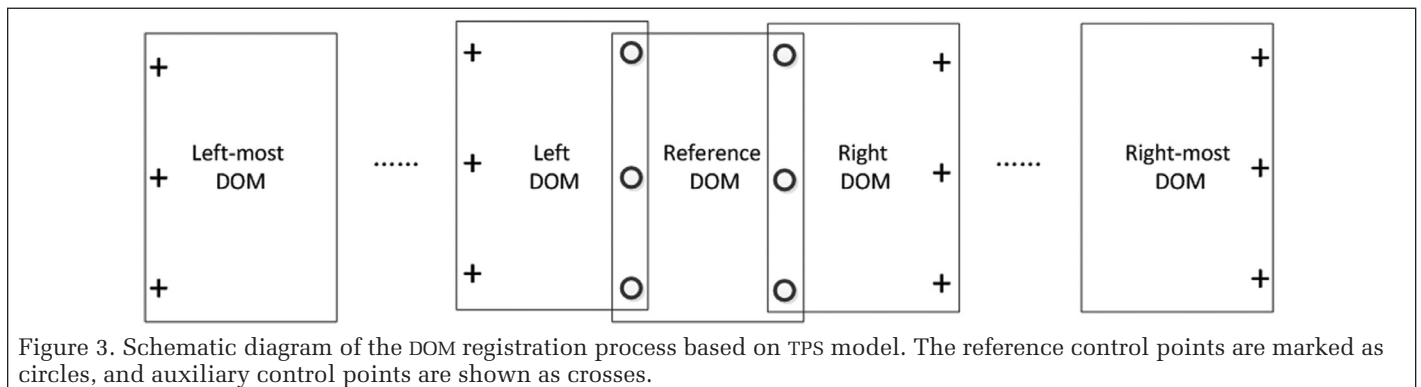


Figure 3. Schematic diagram of the DOM registration process based on TPS model. The reference control points are marked as circles, and auxiliary control points are shown as crosses.

of the auxiliary control point remain unchanged. Other coordinates in the target DOM were smoothly transformed using the calculated TPS coefficients.

The whole registration process can be implemented simultaneously with all the control points matched in advance. To be specific, the homologous points between every two subarea DOMs are obtained first as reference or auxiliary control points. These control points will be unchanged during the whole registration process. Then the TPS model for every target DOM is established in parallel with the achieved control points. Thus, the registration of every target DOM can be implemented independently and simultaneously. Finally, the DOM mosaic of the entire landing area was generated in high geometric consistency.

Results and Analyses

Planar Block Adjustment Results

The whole planned Chang'e-5 landing area was partitioned into 10 subareas in longitude. The subareas covered approximately 3° in longitudinal direction with an overlap of 1°. The 10 subareas from left to the right were named Parts 1 to 10. The quantity of LROC NAC images in every subarea is displayed in Table 1

together with the control point and tie point numbers for the planar block adjustment. The borders of each subarea overlapping on the selected NAC images are depicted in Figure 4.

The planar block adjustment was performed on the 10 subareas separately, and the results are shown in Table 2. The unit of all the precision assessment results is one NAC image pixel, which is set to be 1.5 m in this research. The control point precision was evaluated in image space by the RMS errors between the back-projected coordinates and the measured-image coordinates. As shown in Table 2, the RMS errors for the control points are approximately 27 NAC image pixels on average, which is about one grid cell size of the SLDEM2015 in the research area, with the maximum error no more than two grid cell size, reflecting that the subarea DOMs are connected well to the SLDEM2015. As for the tie points, the RMS errors were also measured by the difference between the matched image coordinates and the back-projected image coordinates. The RMS errors of tie points, as shown in Tables 1 and 2, are approximately one-half of an NAC image pixel in every part, which indicates that the geometric consistencies of NAC images in the subareas were effectively improved after planar block adjustment.

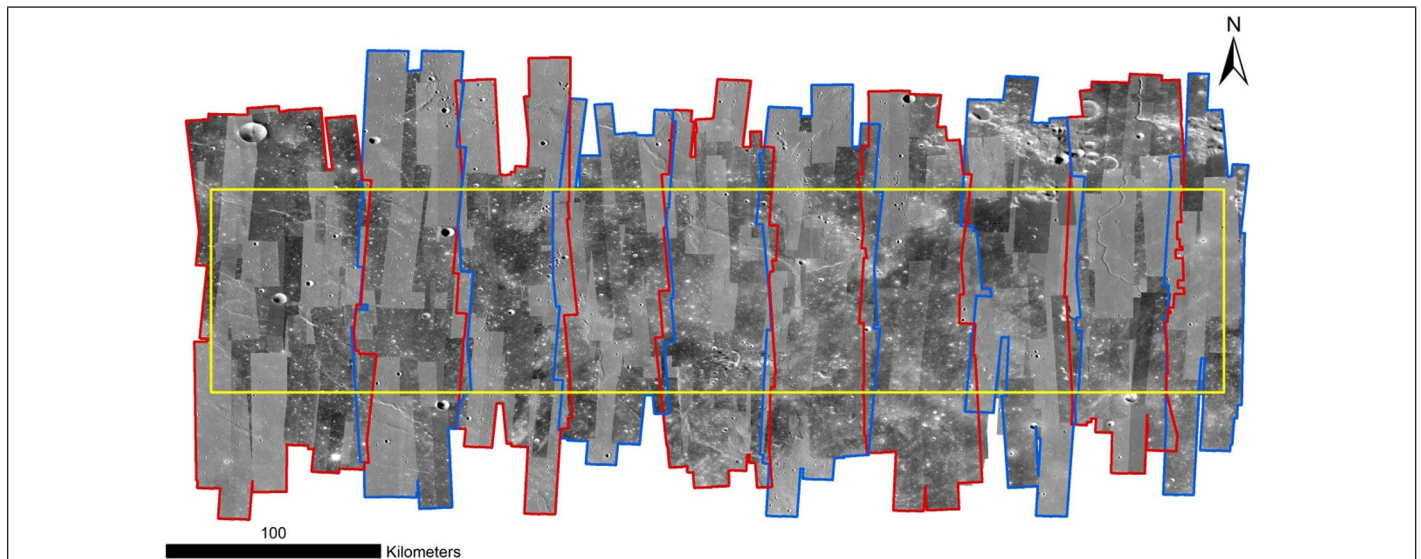


Figure 4. Footprints of all the selected LROC NAC images and the borders of the 10 subareas. Red and blue colors are used alternately for distinguishing the subarea borders. The yellow rectangle represents the planned landing area of Chang'e-5.

Table 1. Image numbers, control point, and tie point numbers in the ten subareas.

Subarea ID	Part 1	Part 2	Part 3	Part 4	Part 5	Part 6	Part 7	Part 8	Part 9	Part 10
Image number	111	71	73	56	93	84	74	54	85	49
Control point number	8	10	11	10	9	11	11	8	9	8
Tie point number	46 386	39 279	49 005	47 174	48 243	48 253	51 425	35 485	41 601	31 148

Table 2. Control point and tie point precisions of the planar block adjustment in ten subareas. The unit is an NAC image pixel assumed to be 1.5 m.

Subarea ID	RMS Errors of Control Points (Pixel)			Maximum Errors of Control Points (Pixel)			RMS Errors of Tie Point (Pixel)			Maximum Errors of Tie Point (Pixel)		
	x	y	xy	x	y	xy	x	y	xy	x	y	xy
Part 1	13.10	19.41	23.42	1.71	38.42	38.46	0.33	0.48	0.58	0.33	-3.31	3.33
Part 2	19.18	21.75	29.00	27.49	-25.76	37.68	0.37	0.45	0.58	0.75	-2.84	2.93
Part 3	17.75	19.81	26.60	21.92	37.94	43.82	0.46	0.62	0.77	0.11	-2.83	2.83
Part 4	17.70	13.23	22.10	34.60	9.24	35.81	0.17	0.30	0.34	-0.33	1.43	1.47
Part 5	18.71	13.71	23.20	32.50	3.14	32.65	0.16	0.18	0.24	2.80	0.24	2.81
Part 6	17.08	13.04	21.49	17.07	-21.94	27.80	0.23	0.36	0.43	2.53	-0.26	2.54
Part 7	23.44	15.52	28.11	40.90	11.76	42.56	0.26	0.38	0.46	-1.85	1.10	2.15
Part 8	32.13	19.30	37.48	43.67	-35.92	56.54	0.41	0.43	0.59	-3.40	1.50	3.72
Part 9	36.41	8.10	37.30	40.78	-11.34	42.33	0.26	0.21	0.33	2.45	0.50	2.50
Part 10	19.37	15.39	24.74	36.83	-13.60	39.26	0.25	0.51	0.57	0.50	-2.75	2.80

After planar block adjustment, the DOMs of the NAC images were automatically generated via ortho-rectification. The block adjustment results can also be assessed by the geometric deviations between these DOMs. Figure 5 displays three examples of the positional deviations of two neighboring NAC DOMs before and after block adjustment. The upper three subfigures show parts of the DOMs rectified using the original RFMs, while the lower three are the DOMs produced from the same images but with the block adjustment–refined RFMs. The three groups of examples come from Part 1 ((a) and (d)), Part 5 ((b) and (e)), and Part 10 ((c) and (f)), respectively. It can be seen that in subfigures (a), (b), and (c) that there exist up to 100-m geometric deviations that are almost completely removed by the block adjustment as depicted in subfigures (e), (f), and (g).

Figure 6 compares the positional differences between NAC DOMs and SLDEM2015 before (subfigures (a), (b), and (c)) and after (subfigures (d), (e), and (f)) the planar block adjustment. The NAC DOMs in subfigures (a) and (d) are part of m1221740903r in Part 1, (b) and (e) are part of m1175809506l in Part 5, and (c) and (f) are part of m1145135367l in Part 10. It can be seen that the geometric differences before block adjustment are about two grid sizes of the SLDEM. After block adjustment processing, these deviations are almost completely corrected with the manually selected control points.

Seamless DOM mosaics were generated for each subarea via the process of planar block adjustment, image ortho-rectification, grayscale balancing, and final DOM mosaicking. The LROC WAC mosaic product was chosen as the reference for histogram matching–based grayscale balancing. Most of the time, the seam lines were automatically extracted. However,

if two adjacent images had obvious illumination difference, the seam lines would need some manual editing to guarantee natural transition of the grayscale.

Overall Block Adjustment Evaluation

Although mapping with partitions is widely used when dealing with a large amount of data or large-area mapping, there is little research on the evaluation of the attainable accuracy between the overall block adjustment and the subareas block adjustment. In this article, we gave a specific analysis on this issue using LROC NAC images in our study area.

The block adjustment using the same control points and tie points of the subarea blocks was performed with all the images involved in the subarea block adjustment, the results of which are shown in Table 3. It demonstrates that the RMS errors of tie points can achieve subpixel-level accuracy in both subarea and overall block adjustment in our study case. But the maximum error of the tie points from the overall adjustment is almost twice the maximum errors from the subarea block adjustment. This indicates that a partition can improve the quality of DOM and mosaicking products. Both RMS and maximum errors show that the precision at control points decreased remarkably. This may be partially due to the insufficient precision of control points selected from a lower-resolution reference. To rectify the orbital images to the reference DEM for synergetic analysis of different data sets in further applications, the orbital images should be well coregistered to the reference DEM. In this perspective, the partition strategy for planar block adjustment is meaningful and effective.

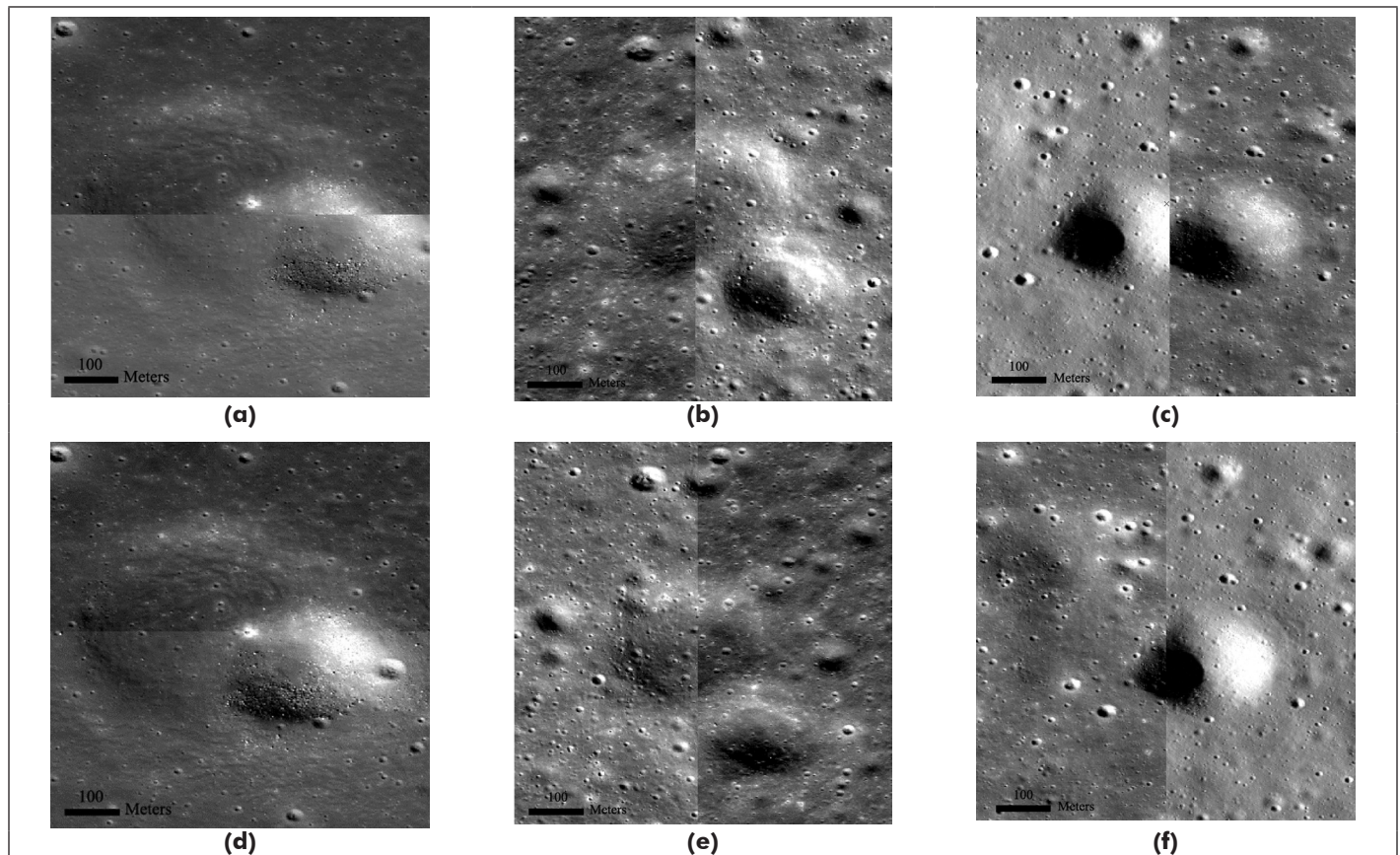


Figure 5. The geometric consistency comparisons between two neighboring DOMs. The upper three subfigures are the DOMs generated using original RFMs, and the lower three are the DOMs rectified by the planar block adjustment refined RFMs. Subfigures (a) and (d) are part of m1221740903r and m1191136940l in Part 1, (b) and (e) are part of m1208769920r and m1175809506l in Part 5, and (c) and (f) are part of m181502892le and m1145135367l in Part 10.

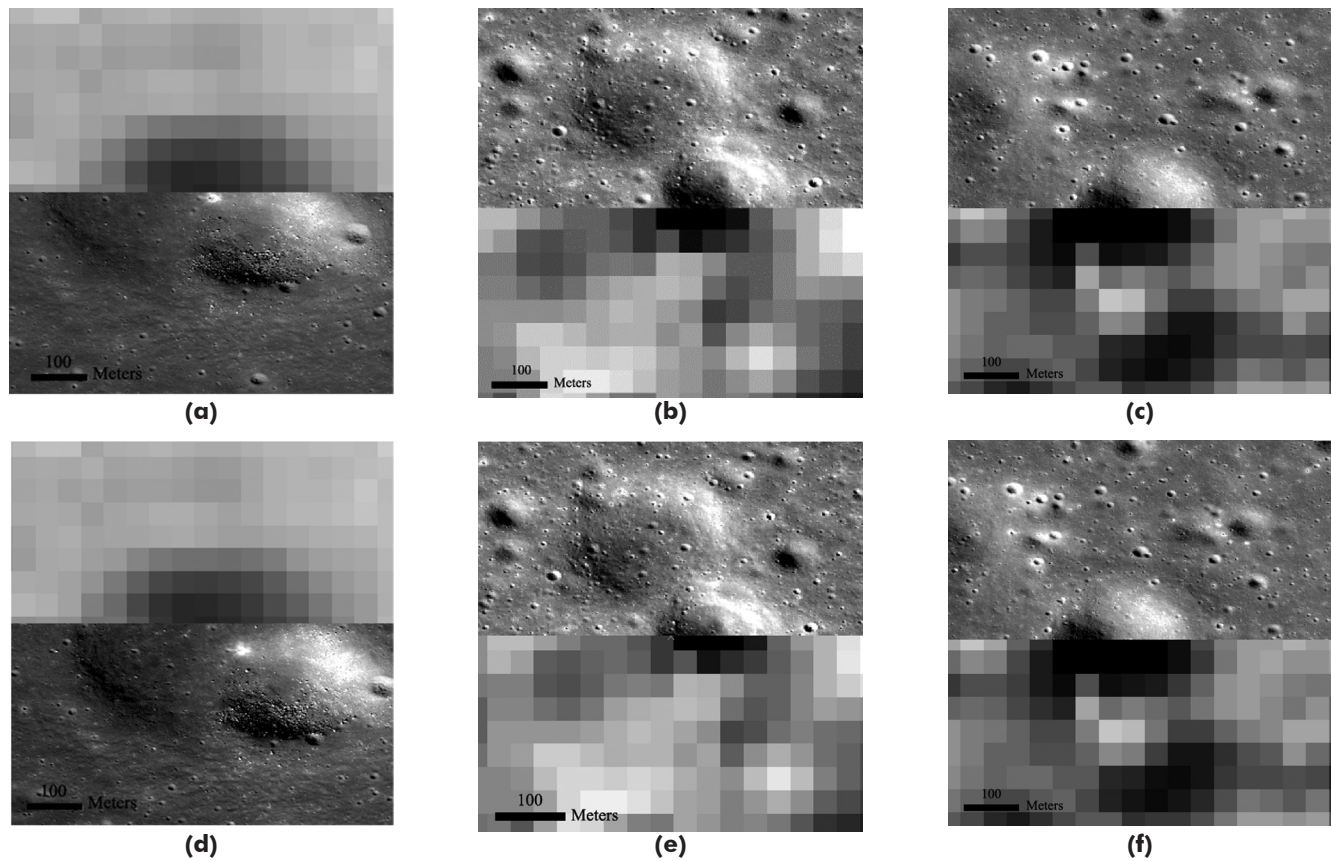


Figure 6. The geometric differences between NAC DOMs and SLDEM2015 before (upper three) and after (lower three) the planar block adjustment. The NAC DOMs in subfigures (a) and (d) are part of m1221740903r in Part 1, (b) and (e) are part of m1175809506l in Part 5, and (c) and (f) are part of m1145135367l in Part 10.

Table 3. Image numbers, control point, and tie point numbers and control point and tie point precisions of the overall block adjustment using all the selected NAC images involved in the subarea block adjustment. The unit for precision assessment is an NAC image pixel assumed to be 1.5 m.

Image Number	Control Point number	Tie Point Number	RMS Errors of Control Points (Pixel)			Maximum Errors of Control Points (Pixel)			RMS Errors of Tie Point (Pixel)			Maximum Errors of Tie Point (Pixel)		
			x	y	xy	x	y	xy	x	y	xy	x	y	xy
750	95	437 999	23.69	26.13	35.27	49.87	78.93	93.37	0.27	0.37	0.46	0.94	5.62	5.7

TPS-Based DOM Registration Results

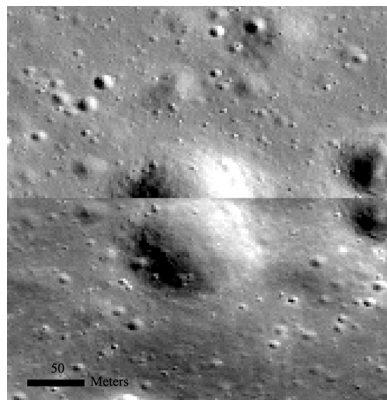
Due to the limited resolution of the SLDEM2015 compared with the LROC NAC images, geometric inconsistencies still exist between the seamlessly mosaicked adjacent subarea DOMs. The upper two subfigures in Figure 7 show examples of the geometric inconsistencies between Part 1 and 2 as well as Part 9 and 10 mosaicked DOMs, which were effectively reduced by the image registration process based on the TPS model as indicated in subfigures (c) and (d) in Figure 7. The registration was conducted subarea by subarea using the procedure detailed in the section “TPS-Based Large-Area Image Registration.” A quantitative evaluation of the registration results can also be realized by measuring the differences of the check point pair coordinates between any two overlapping subarea DOM mosaics. Parts 1 and 2 are taken as examples. Evenly distributed check point pairs were automatically matched in the overlapping region, as shown in Figure 8.

The deviations of the check point coordinates in the latitudinal and longitudinal directions are listed in Table 4. After the TPS-based registration, the planar deviations are reduced to about 1 pixel, and the largest difference is 2.69 m, which is no more than 2 pixels of the output DOM, reflecting a high-precision registration.

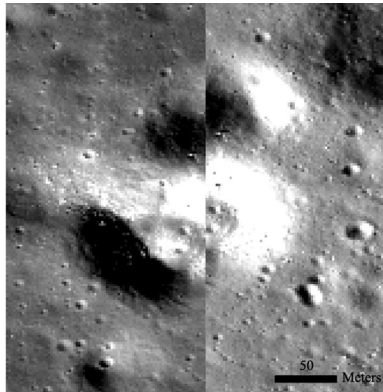
Landing Area DOM and Potential Applications

After subarea planar block adjustment and TPS-based image registration of the subarea DOMs, a seamless DOM mosaic of the entire Chang’e-5 planned landing area was produced. The generated radiometrically homogeneous and geometrically seamless DOM mosaic is shown in Figure 9 (zoomed-out view). This final DOM mosaic has the image size of 224 721 columns and 44 945 rows with a ground sample distance of 1.5 m.

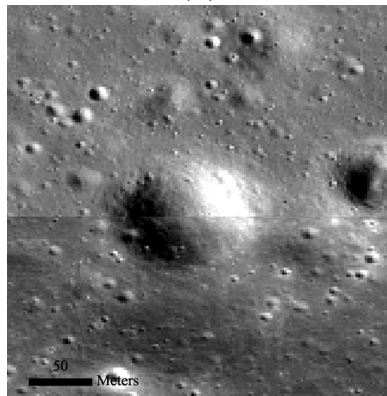
This high-resolution 10-gigapixel DOM has many potential applications for detailed morphological and geological studies. For example, using the high-resolution map, craters can be precisely measured to determine the age of surface units (Michael and Neukum 2010); small, particularly fresh craters (e.g., flat-bottomed, central-mound, and concentric craters) can be used to estimate the depth of the lunar regolith (Bart *et al.* 2011; Di *et al.* 2016); rocks/boulders on the ejecta of a crater can be identified and the spatial density used to estimate the formation time of the crater (Li *et al.* 2017); and so on. More important, distribution pattern analyses of crater rays, crater chains, and boulders are significant in helping identify source locations of the exposed features (e.g., rock and soil samples to be collected by the lander), which will directly contribute to the major scientific objective of the sample return mission.



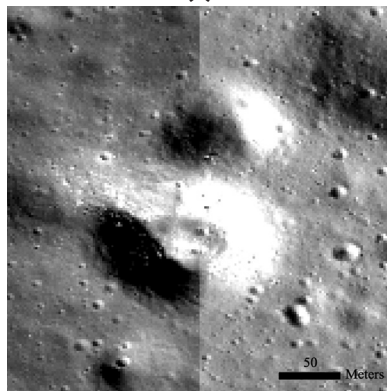
(a)



(b)



(c)



(d)

Figure 7. The positional difference comparisons between two neighboring subarea DOMs before (upper two) and after (lower two) the image registration process based on the TPS model. Subfigures (a) and (c) are from the overlapping area of Parts 1 and 2, and (b) and (d) are from the overlapping area of Parts 9 and 10.

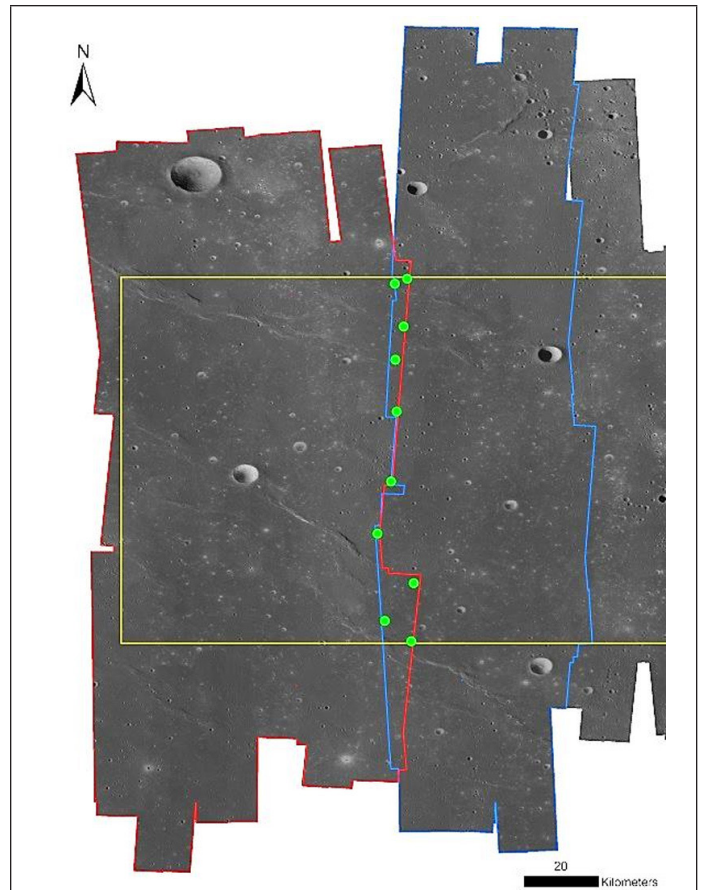


Figure 8. Check points (green circles) between Parts 1 and 2 subarea DOM mosaics for precision evaluation of the TPS-based image registration. The red polygon is the border of Part 1, the blue polygon is the border of Part 2, and the yellow rectangle shows part of the planned landing area of Chang'e-5.

Table 4. TPS-based DOM registration precision between Part 1 and Part 2 subarea DOM mosaics (1.5 m/pixel). “Lat Diff” and “Long Diff” represent the coordinate differences in latitude and longitude directions, respectively; “chk” represents check point.

Chk ID	Before DOM Registration (m)			After DOM Registration (m)		
	Long Diff	Lat Diff	Planar Diff	Long Diff	Lat Diff	Planar Diff
chk1	4.69	-14.30	15.05	1.62	-1.26	2.05
chk2	15.72	-15.87	22.34	0.42	-0.61	0.74
chk3	-11.05	-21.96	24.58	0.96	-0.56	1.11
chk4	11.68	-16.57	20.27	-1.58	-2.17	2.69
chk5	-4.29	17.76	18.27	1.13	0.79	1.38
chk6	4.56	24.05	24.48	0.00	-1.20	1.20
chk7	-10.15	29.91	31.58	0.22	0.39	0.45
chk8	6.08	32.38	32.94	0.66	0.37	0.75
chk9	15.63	10.85	19.02	-0.37	1.26	1.32
chk10	6.08	-9.95	11.66	-0.78	0.42	0.88

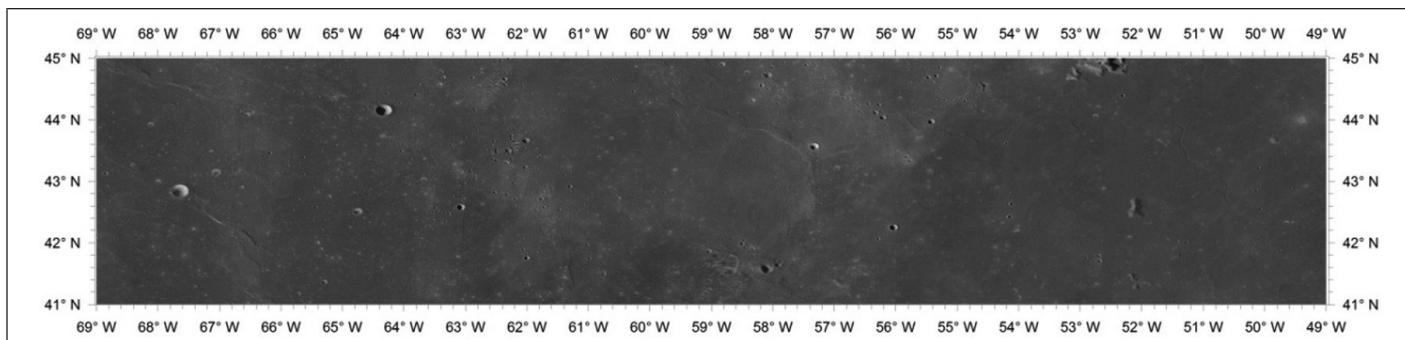


Figure 9. Produced seamless DOM mosaic of the Chang'e-5 planned landing area.

Conclusions

To solve the problems of large-area controlled seamless DOM production using LROC NAC images, a systematic method consisting of two stages of data processing is developed in this study. First, the RFM-based planar block adjustment is used to improve the relative positional consistencies of the LROC NAC images to the subpixel level and at the same time tie the NAC images to the control source (SLDEM2015). Second, a TPS-based image registration is used to reduce the geometric inconsistencies between two neighboring subarea DOM mosaics and ensures final DOM being seamlessly mosaicked throughout the entire area.

A high-resolution seamless DOM mosaic is produced with the proposed two-stage method for the Chang'e-5 planned landing area using 765 NAC images. Consequently, the tie point RMS errors are all approximately one-half pixel, showing satisfactory geometric consistencies among NAC images. The control point RMS errors were approximately one grid cell size of SLDEM2015, which means that the produced DOM has been registered to SLDEM2015 with high precision. After DOM registration with the TPS model, the planar precision is mostly smaller than one pixel in the output DOM. The resultant DOM mosaic, covering 49°–69° west longitude and 41°–45° north latitude, has an image size of 224 721 columns \times 44 945 rows with a ground sample distance of 1.5 m. This high-resolution DOM is of great importance for detailed morphological and geological analysis of the Chang'e-5 landing area. The developed method is applicable to high-resolution mapping of other large areas on the lunar surface using LROC NAC images.

Acknowledgments

This work was supported by the Key Research Program of the Chinese Academy of Sciences (grant no. XDPB11) and the National Natural Science Foundation of China (grant nos. 41671458, 41590851, and 41771490). We thank all those who worked on the Planetary Data System archive to make the LRO imagery and SLDEM2015 publicly available.

References

Archinal B. A., E. Lee, L. Weller, J. Richie, K. Edmundson, M. Robinson, E. Speyerer, A. K. Boyd, E. Bowman-Cisneros, R. Wagner and A. V. Nefian. 2015. Status of geodetically controlled high-resolution LROC polar mosaics. Page 1571 in *Proceedings of 46th Lunar and Planetary Science Conference*, held in The Woodlands, Tex., 16–20 March 2015.

Arizona State University. 2011. WAC Global Morphologic Map. <http://wms.lroc.asu.edu/lroc/view_rdr/WAC_GLOBAL> Accessed 10 April 2018.

Barker, M. K., E. Mazarico, G. A. Neumann, M. T. Zuber, J. Haruyama and D. E. Smith. 2016. A new lunar digital elevation model from the Lunar Orbiter Laser Altimeter and SELENE Terrain Camera. *Icarus* 273:346–355.

Bart, G. D., R. D. Nickerson, M. T. Lawder and J. Melosh. 2011. Global survey of lunar regolith thickness from LROC images. *Icarus* 215(2):485–490.

Burns, K. N., E. J. Speyerer, M. S. Robinson, T. Tran, M. R. Rosiek, B. A. Archinal and E. Howington-Kraus. 2012. Digital elevation models and derived products from LROC NAC stereo observations. Pages 483–488 in *Proceedings of 22nd Congress of International Archives of the Photogrammetry, Remote Sensing and Spatial Information Sciences—ISPRS Archives*, held in Melbourne, Australia, 25 August–1 September 2012.

Data Publishing and Information Service System of China' Lunar Exploration Project. 2018. <http://moon.bao.ac.cn/searchOrder_dataSearch.search> Accessed 2 July 2018.

Di, K., M. Jia, X. Xin, B. Liu, Z. Liu, M. Peng and Z. Yue. 2018. High resolution seamless DOM generation over Chang'e-5 landing area using LROC NAC images. Pages 271–276 in *Proceedings of 2018 ISPRS TC III Mid-term Symposium "Developments, Technologies and Applications in Remote Sensing,"* held in Beijing, China, 7–10 May.

Di, K., Y. Liu, B. Liu, M. Peng and W. Hu. 2014. A self-calibration bundle adjustment method for photogrammetric processing of Chang'e-2 stereo lunar imagery. *IEEE Transactions on Geoscience and Remote Sensing* 52(9):5432–5442.

Di, K., S. Sun, Z. Yue and B. Liu. 2016. Lunar regolith thickness determination from 3D morphology of small fresh craters. *Icarus* 267:12–23.

Gbtimes. 2017. China confirms landing site for Chang'e-5 Moon sample return. <<https://gbtimes.com/china-confirms-landing-site-change-5-moon-sample-return>> Accessed 10 April 2018.

Gwinner, K., R. Jaumann, E. Hauber, H. Hoffman, C. Heipke, J. Oberst, G. Neukum, V. Ansan, J. Bostelmann, A. Dumke, S. Elgner, G. Erkeling, F. Fueten, H. Hiesinger, N. M. Hoekzema, E. Kersten, D. Loizeau, K.-D. Matz, P. C. McGuire, V. Mertens, G. Michael, A. Pasewaldt, P. Pinet, F. Preusker, D. Reiss, T. Roatsch, R. Schmidt, F. Scholten, M. Spiegel, R. Stesky, D. Tirsh, S. van Gasselt, S. Walter, M. Wählisch and K. Willner. 2016. The high resolution stereo camera (HRSC) of Mars Express and its approach to science analysis and mapping for Mars and its satellites. *Planetary and Space Science* 126:93–138.

Gwinner, K., F. Scholten, F. Preusker, S. Elgner, T. Roatsch, M. Spiegel, R. Schmidt, J. Oberst, R. Jaumann and C. Heipke. 2010. Topography of Mars from global mapping by HRSC high-resolution digital terrain models and orthoimages: Characteristics and performance. *Earth and Planetary Science Letters* 294(3):506–519.

Haase, I., J. Oberst, F. Scholten, M. Wählisch, P. Gläser, I. Karachevtseva and M. S. Robinson. 2012. Mapping the Apollo 17 landing site area based on Lunar Reconnaissance Orbiter Camera images and Apollo surface photography. *Journal of Geophysical Research: Planets* 117(E00H20):1–8.

Haase, I., M. Wählisch, P. Gläser, J. Oberst and M. S. Robinson. 2014. Apollo 17 landing site: A cartographic investigation of the Taurus-Littrow Valley based on LROC NAC imagery. Pages 1–12 in *Proceedings of European Planetary Science Congress*, held in Cascais, Portugal 7–12 September 2014.

- Henriksen, M. R., M. R. Manheim, K. N. Burns, P. Seymour, E. J. Speyerer, A. Deran, A. K. Boyd, E. Howington-Kraus, M. R. Rosiek, B. A. Archinal and M. S. Robinson. 2016. Extracting accurate and precise topography from LROC narrow angle camera stereo observations. *Icarus* 283:122–137.
- Klem, S. M., M. R. Henriksen, J. Stopar, A. Boyd and M. S. Robinson. 2014. Controlled LROC narrow angle camera high resolution mosaics. Page 2885 in *Proceedings of 45th Lunar and Planetary Science Conference*, held in The Woodlands, Tex., 17–21 March 2014.
- Kokhanov, A. A., I. P. Karachevtseva, A. E. Zubarev, V. Patraty, Z. F. Rodionova and J. Oberst. 2017. Mapping of potential lunar landing areas using LRO and SELENE data. *Planetary and Space Science*, in press. <<https://doi.org/10.1016/j.pss.2017.08.002>>
- Lee, E. M., L. A. Weller, J. O. Richie, B. L. Redding, J. R. Shinaman, K. Edmundson, B. A. Archinal, T. M. Hare and R. L. Fergason. 2012. Controlled polar mosaics of the Moon for LMMP by USGS. Page 2507 in *Proceedings of 43rd Lunar and Planetary Science Conference*, held in The Woodlands, Tex., 19–23 March 2012.
- Li, C. L., J. J. Liu, X. Ren, L. L. Mous, Y. L. Zou, H. B. Zhang, C. Lü, J. Z. Liu, W. Zuo, Y. Su, W. B. Wen, W. Bian, B. C. Zhao, J. F. Yang, X. D. Zou, M. Wang, C. Xu, D. Q. Kong, X. Q. Wang, F. Wang, L. Geng, Z. B. Zhang, L. Zheng, X. Y. Zhu, J. D. Li and Z. Y. Ouyang. 2010. The global image of the Moon obtained by the Chang' E-1: Data processing and lunar cartography. *Science China: Earth Science*. 53(8):1091–1102.
- Li, C., X. Ren, J. Liu, F. Wang, W. Wang, W. Yan and G. Zhang. 2015. A new global and high resolution topographic map product of the Moon from Chang'e-2 image data. Page 1638 in *Proceedings of 46th Lunar and Planetary Science Conference*, held in The Woodlands, Tex., 16–20 March 2015.
- Li, Y., A. T. Basilevsky, M. Xie and W.-H. Ip. 2017. Correlations between ejecta boulder spatial density of small lunar craters and the crater age. *Planetary and Space Science*, in press. <<https://doi.org/10.1016/j.pss.2017.08.007>>
- Liu, B., M. Jia, K. Di, J. Oberst, B. Xu and W. Wan. 2017. Geopositioning precision analysis of multiple image triangulation using LROC NAC lunar images. *Planetary and Space Science*, in press. <<https://doi.org/10.1016/j.pss.2017.07.016>>
- Liu, B., B. Xu, K. C. Di and M. N. Jia. 2016. A solution to low fitting precision of planetary orbiter images caused by exposure time changing. Pages 441–448 in *Proceedings of 23rd ISPRS Congress, Commission IV*, held in Prague, Czech Republic, 12–19 July 2016.
- Michael, G. G. and G. Neukum. 2010. Planetary surface dating from crater size–frequency distribution measurements: Partial resurfacing events and statistical age uncertainty. *Earth and Planetary Science Letters* 294(3–4):223–229.
- Mazarico, E., D. D. Rowlands, G. A. Neumann, D. E. Smith, M. H. Torrence, F. G. Lemoine and M. T. Zuber. 2012. Orbit determination of the Lunar Reconnaissance Orbiter. *Journal of Geodesy* 86 (3):193–207.
- Moratto, Z. M., M. J. Broxton, R. A. Beyer, M. Lundy and K. Husmann. 2010. Ames Stereo Pipeline, NASA's open source automated stereogrammetry software. Page 2364 in *Proceedings of 41st Lunar and Planetary Science Conference*, held in The Woodlands, Tex., 1–5 March 2010.
- NAIF. 2014. Lunar Reconnaissance Orbiter Camera (LROC) Instrument Kernel v18. <http://naif.jpl.nasa.gov/pub/naif/pds/data/lro-l-spice-6-v1.0/lrosp_1000>. Accessed 10 April 2018.
- National Aeronautics and Space Administration. 2011. LRO Camera Team Release High Resolution Global Topographic Map of Moon. <http://www.nasa.gov/mission_pages/LRO/news/lro-topo.html>. Accessed 10 April 2018.
- National Aeronautics and Space Administration, Goddard Space Flight Center, and Arizona State University. 2014. 681 Gigapixels. <<http://lroc.sese.asu.edu/posts/738>>. Accessed 10 April 2018.
- Ouyang, Z., Y. Zou and C. Li. 2004. The scientific objectives of Chinese First Lunar Exploration Project. *Science and Technology*. 1–2.
- Planetary Data System. 2014. Processing of Lunar Reconnaissance Orbiter Camera Narrow Angle Camera Image Frames with ISIS 3. <https://pds-imaging.jpl.nasa.gov/documentation/LROC_NAC_CreateCDRs_w_ISIS_Feb14.pdf>. Accessed 10 April 2018.
- Preusker, F., A. Stark, J. Oberst, K.-D. Matz, K. Gwinner, T. Roatsch and T. R. Watters. 2017. Toward high-resolution global topography of Mercury from MESSENGER orbital stereo imaging: A prototype model for the H6 (Kuiper) Quadrangle. *Planetary and Space Science*. 142:26–37.
- Robinson, M. S., S. M. Brylow, M. Tschimmel. 2010. Lunar Reconnaissance Orbiter Camera (LROC) instrument overview. *Space Science Review* 150(1–4):81–124.
- Robinson, M. S., A. S. McEwen, E. Eliason, E. M. Lee, E. Malaret and P. G. Lucey. 1999. Clementine UVIS global mosaic: A new tool for understanding the lunar crust. Page 1931 in *Proceedings of 30th Lunar and Planetary Science Conference*, held in The Woodlands, Tex., 14–19 March 1999.
- Shen, X., B. Liu and Q. Q. Li. 2017. Correcting bias in the rational polynomial coefficients of satellite imagery using thin-plate smoothing splines. *ISPRS Journal of Photogrammetry and Remote Sensing* 125:125–131.
- Tran, T., M. R. Rosiek, R. A. Beyer, S. Mattson, E. Howington-Kraus, M. Robinson, B. A. Archinal, K. Edmundson, D. Harbour and E. Anderson. 2010. Generating digital terrain models using LROC NAC images. Pages 1-7 in *Proceedings of ASPRS/CaGIS 2010 Fall Specialty Conference*, held in Orlando, Fla., 15–19 November 2010.
- Wagner, R. V., M. S. Robinson and LROC Team. 2016. Design and processing of the Lunar North Pole Mosaic. Page 1582 in *Proceedings of 47th Lunar and Planetary Science Conference*, held in The Woodlands, Tex., 21–25 March 2016.
- Wagner, R. V., E. J. Speyerer, M. S. Robinson and LROC Team. 2015. New mosaicked data products from the LROC team. Page 1473 in *Proceedings of 46th Lunar and Planetary Science Conference*, held in The Woodlands, Tex., 16–20 March 2015.
- Wahba, G. 1990. *Spline Models for Observational Data*. Philadelphia: Society for Industrial and Applied Mathematics.
- Wu, B., F. Li, L. Ye, S. Qiao, J. Huang, X. Wu and H. Zhang. 2014. Topographic modeling and analysis of the landing site of Chang'e-3 on the Moon. *Earth and Planetary Science Letters* 405:257–273.
- Wu, B. and W. C. Liu. 2017. Calibration of boresight offset of LROC NAC imagery for precision lunar topographic mapping. *ISPRS Journal of Photogrammetry and Remote Sensing* 128:372–387.
- Wu B., H. Zeng and H. Hu. 2018. Illumination invariant feature point matching for high-resolution planetary remote sensing images. *Planetary and Space Science* 152:45–54.
- Yue, Z., G. G. Michael, K. Di and J. Liu. 2017. Global survey of lunar wrinkle ridge formation times. *Earth and Planetary Science Letters* 477:14–20.
- Zhang, F., M. H. Zhu and Y. L. Zou. 2016. Late stage Imbrium volcanism on the Moon: Evidence for two source regions and implications for the thermal history of Mare Imbrium. *Earth and Planetary Science Letters* 445:13–27.